



HAL
open science

Label-free single nanoparticle identification and characterization in demanding environment, including infectious emergent virus

Minh-Chau Nguyen, Peter Bonnaud, Rayane Dibs, Guillaume Maucort, Sébastien Lyonnais, Delphine Muriaux, Pierre Bon

► To cite this version:

Minh-Chau Nguyen, Peter Bonnaud, Rayane Dibs, Guillaume Maucort, Sébastien Lyonnais, et al.. Label-free single nanoparticle identification and characterization in demanding environment, including infectious emergent virus. *Small*, In press, pp.2304564. 10.1002/sml.202304564 . hal-03926804v2

HAL Id: hal-03926804

<https://hal.science/hal-03926804v2>

Submitted on 28 Nov 2023

HAL is a multi-disciplinary open access archive for the deposit and dissemination of scientific research documents, whether they are published or not. The documents may come from teaching and research institutions in France or abroad, or from public or private research centers.

L'archive ouverte pluridisciplinaire **HAL**, est destinée au dépôt et à la diffusion de documents scientifiques de niveau recherche, publiés ou non, émanant des établissements d'enseignement et de recherche français ou étrangers, des laboratoires publics ou privés.

Label-free single nanoparticle identification and characterization in demanding environment, including infectious emergent virus

Minh-Chau Nguyen, Peter Bonnaud, Rayane Dibsy, Guillaume Maucort, Sébastien Lyonnais, Delphine Muriaux, Pierre Bon

Minh-Chau Nguyen, Peter Bonnaud, Pierre Bon

Université de Limoges, CNRS, XLIM, UMR 7252, F-87000 Limoges, France

Email : minh-chau.nguyen@cnrs.fr, pierre.bon@cnrs.fr

Rayane Dibsy, Delphine Muriaux

IRIM (Institut de Recherche en Infectiologie de Montpellier), Université de Montpellier, UMR 9004 CNRS, Montpellier

Guillaume Maucort

Laboratoire Photonique Numérique et Nanosciences, University of Bordeaux, F-33400

Talence, France; LP2N UMR 5298, Institut d'Optique Graduate School, CNRS, F-33400

Talence, France

Sébastien Lyonnais, Delphine Muriaux

CEMIPAI, Université de Montpellier, CNRS, UAR 3725 CNRS, Montpellier

Keywords: label-free single nanoparticle identification, single nanoobject metrology, infectious virus imaging, quantitative phase microscopy

Abstract

Unknown particle screening -including virus and nanoparticles- are keys in medicine, industry and also in water pollutant determination. Here we introduce RYtov Microscopy for Nanoparticles Identification (RYMINI), a staining-free, non-invasive and non-destructive optical approach that is merging holographic label-free 3D tracking with high-sensitivity quantitative phase imaging into a compact optical setup. Dedicated to the identification and then characterization of single nano-object in solution, it is compatible with highly demanding environments, such as level 3 biological laboratories, with high resilience to external source of mechanical and optical noise. Metrological characterization has been performed at the level of each single particle on both absorbing and transparent particles as well as on immature and infectious HIV, SARS-CoV-2 and extracellular vesicles in solution. We demonstrate the capability of RYMINI to determine the nature, concentration, size, complex refractive index and mass of each single particle without knowledge or model of the particles' response. The system surpasses 90% accuracy for automatic identification between dielectric/metallic/biological nanoparticles and about 80% for intraclass chemical

determination of metallic and dielectric. It falls down to 50-70% for type determination inside the biological nanoparticle's class.

1. Introduction

Having access to metrological parameters on individual nanoparticles is key to characterize the production for food, industry and biomedicine^[1-3] and to identify relevant differences of nature between particles.^[4] In this quest, some measurements could unlock unprecedented comprehension on each individual particles including the molecular content and the density of matter which involve a knowledge on both dimension and weight of each particle in their native environment. Ensemble measurement using dynamic light scattering (DLS) have been proposed^[5,6] to have access to the size of particles –even polydisperse solution- but the intrinsic lack of specificity in the measured signals make this method challenging when nanoparticles with identical size distribution but different nature are in solution (e.g. empty and full extracellular vesicles).

At the single particle level, different techniques have been proposed to label-free measure the particle size. Based on angular distribution of light scattering and/or single-particle tracking (SPT)^[7-21] they can furthermore extract a signal related to the particle refractive index mismatch with the solvent. *A priori* knowledge about the particle light/matter interaction is then required to sort the particles making these methods very challenging when applied simultaneously to both absorbing and transparent nano-objects.

Moreover, when working with nanometer-size bio-objects such as vesicles or viruses, having access to the particle refractive index is not enough to perform acute biological interpretations. At microscopic scale, it has been demonstrated in the 1950's^[22] that light-matter interaction can be converted into mass measurement for biological samples. This approach has been widely applied on optically resolved samples including eukaryotic cells^[23,24] and bacteria.^[25] Different methods of NP and virus mass measurement are introduced by using interferometric light scattering microscopy,^[26,27] electron microscopy,^[28,29] mass spectroscopy,^[30,31] nanometer-scale pores.^[32] However, these methods are only applicable either as destructive method, or for fix particles, or require the presence and the non-destructive interaction of the nanoobject with a lipid bilayer. Miniaturized microfluidic based optical detection and characterization of specific viruses have already been demonstrated^[33,34]. These methods are compatible with biosafety cabinet but they require specific antibody binding, and thus a knowledge on the targeted nano-object.

In this paper, we introduce **RYtov Microscopy for Nanoparticles Identification (RYMINI)** as a novel tool to identify in solution each nanoparticle *via* machine learning allowing us to retrieve its size, concentration, optical attenuation on any type of particles without any possible bias. To do so, we have merged the capability of holography for *(i)* imaging in a single 2D image large 3D volume and for *(ii)* numerical refocusing of each freely diffusing particle,^[35,36] with the high-stability, compactness and sensitivity of self-reference interferometry.^[37,38] This grants an access to the size d of each particle (*via* SPT analysis), its type, and then its complex refractive index $\tilde{n} = n + i \cdot k$ (and so its electric susceptibility

$\chi = \tilde{n}^2 - 1$, or its mass). Moreover, the imaging volume is precisely determined *a posteriori*: a key element to measure particle concentrations in a single-shot acquisition. Our approach is less sensitive in term of detection of small particles than other state-of-the-art demonstrations.^[11,13,14,17,18] However, our aim is to develop a compact setup which is fully-compatible with acquisitions in small and demanding environments including biosafety cabinets in highly confined laboratories. This means the capability to work under uncontrollable and non optical-friendly conditions (vibration, external light background, ...) without compromising the results.

Therefore, we use lateral shearing interferometer^[37-39] which allows stability enhancement and compacity (no reference arm) with respect to holography. Besides, it allows to work in a coherence regime where the volume reconstruction stays accurate over large defocus while decreasing the amount of speckle noise. The use of a fast camera (acquisition frequency of 400Hz) is also an advantage to limit vibration issues and follow small particles. This combined strategy makes possible imaging in demanding environments while keeping sensitive and quantitative measurements. It unlocks the capability to detect, identify and characterize nano-objects, even dangerous for human or environment such as emerging virus or pollutant.

2. Results - Discussion

2.1. Principle

The core idea of our method is to simultaneously measure the size, and the optical intensity and phase response of each nano-object. These three independent measurements grant signal specificity to identify each nanoparticle and determine key metrological information. To do so, we image freely diffusing nanoparticles (in Brownian motion) in their native solution with an optical microscope. The illumination has a controlled spatial and temporal coherence (super-continuum laser, see methods) and each particle –even far from the imaging plane- forms an image on the sensor (Fig 1.a). By using a sensor sensitive to both the phase φ and the intensity I of the light,^[37-39] it is possible for weakly scattering imaged volume to compute a numerical 3D stack from a single 2D hologram (see S1 and Movie S1), the only requirement being to know the illumination wavelength λ and the microscope parameters (pixel size in the object space and numerical aperture). More complex propagation algorithms (based on transport-of-intensity equation) could be envisioned for highly scattering medium.^[40] A large full well capacity camera coupled with short exposition time (<1ms) have been used to remain almost insensitive to ambient light that cannot be avoided in some conditions such as highly confined laboratories (L3 in the case of this study). Figure 1.b gives an overview of the image processing and information harvesting, which will be discussed separately in the following subheadings.

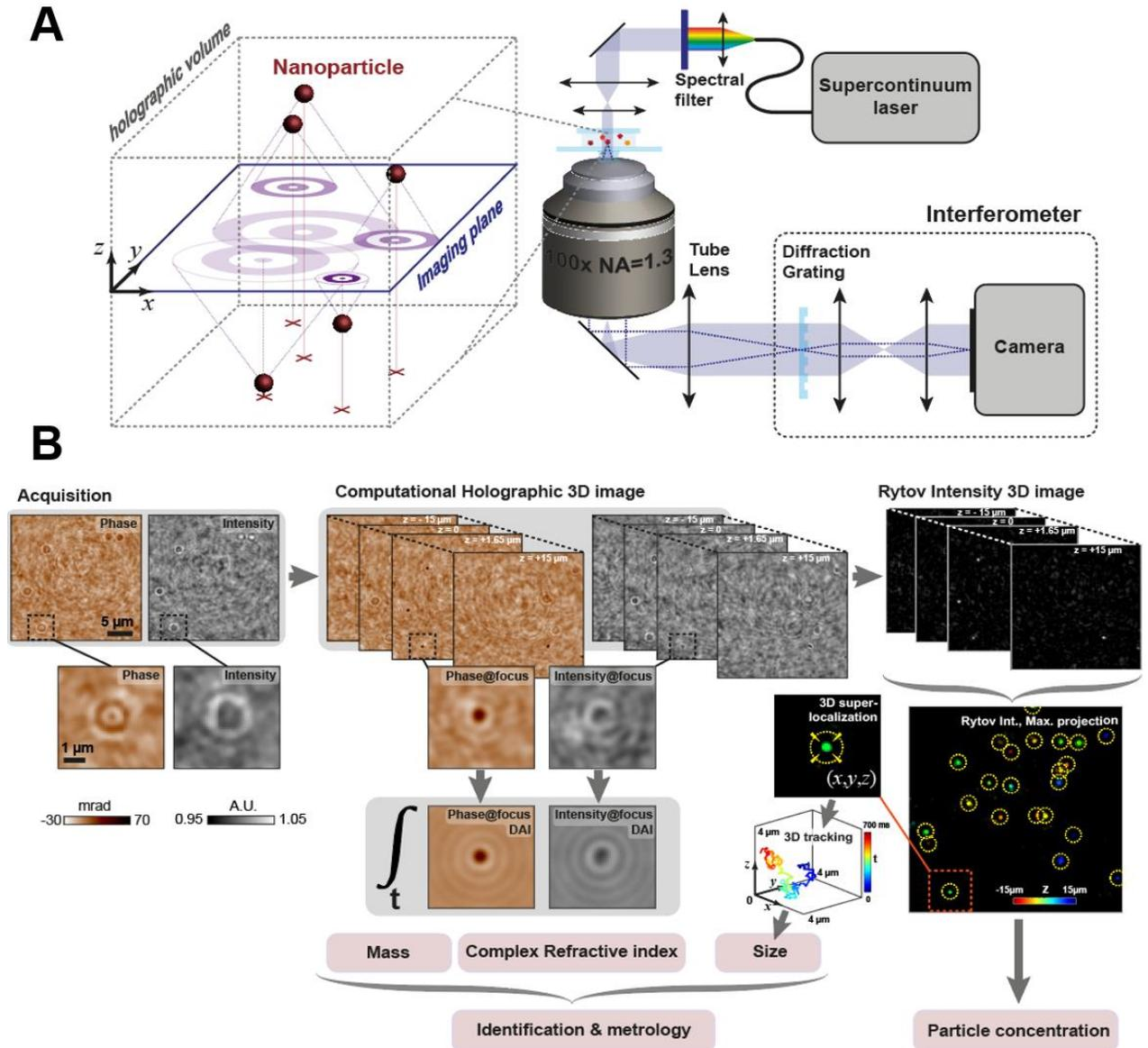


Figure 1: Principle of experiment. (A) Experimental holographic setup. (B) Analysis workflow. From one intensity/phase image couple acquired in single shot, a 3D image stack is computationally generated. The Rytov field intensity is calculated to unlock each particle localization in 3D through. By repeating the procedure at different time points, single particle tracking and signal averaging can be performed to identify and characterize each particle in the solution. DAI stands for Dynamic Average Image (enhancement of the image SNR by temporal averaging of refocused images).

2.2. Dynamic Average Imaging

Successive temporal holograms are then recorded and both the 3D position over time and the intensity and phase images at focus of each particle at each time point are extracted. Though the particles are moving, their images can be numerically refocused and remains static over time at their focal planes. Hence, each particle image can be averaged through time to obtain a maximized signal-to-noise ratio (SNR) intensity and phase image of each freely diffusing particles extracted (see Movie S1). We call this approach **Dynamic Average Imaging (DAI)**.

After DAI, the SNR of both intensity and phase images increases, theoretically by the factor of \sqrt{N} , with N is the number of tracking frames which largely improve the characterization of particles.

2.3. Rytov field for universal localization and quantitative measurements

Variation of intensity and phase images of a particle at different planes depends on particle's nature. Figure 2 shows the simulated images, by Product-of-Convolution,^[41,42] of three different nanoparticles in the focal plane: polystyrene (PS), gold (Au) and silver (Ag). At the working wavelength (i.e. $\lambda=450$ nm), the difference of refractive index between these particles and the medium (water) are respectively:^[43,44] $\Delta\mathbf{n}_{PS} = \mathbf{0.28} + \mathbf{0}i$; $\Delta\mathbf{n}_{Au} = \mathbf{0.05} + \mathbf{1.92}i$ and $\Delta\mathbf{n}_{Ag} = -\mathbf{1.29} + \mathbf{2.65}i$. Thus, their optical response shows 3 different behaviors: PS particle is a dielectric (all information in the phase image), Au is absorbing (all information in the intensity image) and Ag is in-between (information in both intensity and phase images). In order to remain independent in our localization method from the nature of the particle (i.e. dielectric, absorbing or in-between), we have merged the intensity I and the phase signal φ inside a novel observable, called Rytov intensity:

$$I_{Rytov} = |E_{Rytov}|^2 = \left| \frac{i\lambda \cdot n_m}{\pi} \left[\frac{\ln(I)}{2} + i \cdot \varphi \right] \right|^2, \quad (1)$$

with E_{Rytov} the Rytov field (generalized from the polarizability tensor^[45]), and n_m the surrounding medium refractive index (see S2 for more details). Although obtained with a label-free technique, the Rytov intensity image looks very similar from a fluorescence image, in which Rytov intensity reach its maximum when the particle is at the imaging plane, independently from the nature of the imaged particle. Regular and robust localization algorithm can therefore be applied to super-localize in 3D the particle (Gaussian fitting, see methods) without requiring *a priori* knowledge about the particle's nature. The localization precision is far beyond the microscope resolution (e.g. $\lambda/10$ for SARS-CoV-2 virus) within imaging volume of typically 30-pL ($\sim 28 \times 28 \times 30 \mu\text{m}^3$) for dielectric particles (see S3 for complete characterization).

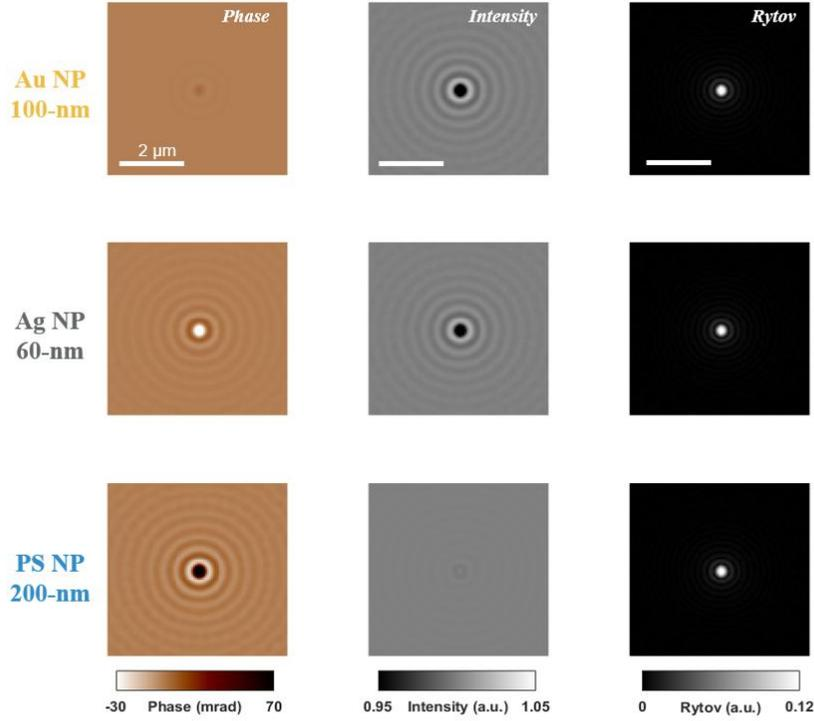


Figure 2: Rytov intensity as universal signal for different optical responses. Simulated images of different particles at focus (considering the bulk refractive index). From top to bottom, 100-nm Au NP, 60-nm Ag NP and 200-nm PS NP. From left to right, phase, intensity and Rytov intensity images. NP sizes are chosen so that their Rytov intensity is comparable.

Noteworthy, the surface integration of Rytov field (SIR) over the whole particle image gives access to the optical volume difference of the particle compared to the medium:

$$\begin{aligned}
 \text{SIR} &= \iint_{x,y} E_{Rytov} dx dy = \frac{\lambda \cdot n_m}{\pi} \iint_{x,y} \left[-\varphi + i \frac{\ln(I)}{2} \right] dx dy \\
 \text{SIR} &= \underbrace{-2 n_m (n - n_m) V_p}_{\text{Re(SIR)}} + i \underbrace{n_m (n' - n'_m) V_p}_{\text{Im(SIR)}} , \quad (2)
 \end{aligned}$$

where, V_p is the particle volume, $n_m + i n'_m$ is the complex refractive index of the medium, λ the working wavelength. From the equation (2), we notice that the real (and imaginary, respectively) part of SIR depends on the real (and imaginary, respectively) part of refractive index and the volume of particles. Therefore, SIR values associated with the NP size (via single particle tracking) can be used to identify the nature of each particle.

Moreover, in order to handle intensity and phase measurements, Rytov field introduces less crosstalk between absorbing and refractive effects than conventional electromagnetic field

calculation proposed in previous NP characterizations^[45] (see S4). This method is thus more direct for particle nature determination and refractive index retrieval.

2.4. Size characterization from Brownian motion and Rytov field

Since the nanoparticles are diffusing following a Brownian motion, according to the Stokes-Einstein law,^[46] the particle hydrodynamic diameter d_h can be obtained *via*:

$$d_h = d + \delta = \frac{k_B T}{6\pi\eta D} , \quad (3)$$

with d the particle diameter, δ the hydrodynamic layer thickness around the particle which depends on the particle and medium nature, k_B the Boltzmann constant, T the fluid temperature, η the viscosity of the fluid and D the diffusion coefficient. The classical way to measure D is to compute the mean squared displacement (MSD) of each nanoparticle trajectory. In addition to a possible more precise MSD evaluation as compared to 2D localization,^[47] the 3D tracking -granted with our holographic method- is more efficient to handle trajectory superposition. The tracking has been performed at high frame rate (400Hz) to ensure accurate evaluation of diffusion coefficient via MSD and minimize the environment vibration influence. To increase the precision of the size evaluation from MSD, we have used a unique characteristic of our method: the signature of the Rytov field for a given particle nature and size which allows us to perform correlation between particles which exhibit the similar Rytov field (see S5). Moreover, our approach unlocks concentration determination without *a priori* knowledge on the particle type: the measurement volume where particles are detected is obtained through the numerical propagation and is automatically adjusted by the signal-to-noise ratio of the detected particles for each type of particles (see S6). This allows unbiased particle concentration measurements by counting the number of detections in this tunable reconstruction volume.

2.5. Automatized single particle identification and characterization

We have developed an architecture based on Vision Transformer,^[48,49] adapted to the complex electromagnetic field,^[50] for automatized particle classification. To identify each particle, the algorithm uses as input parameter the complex Rytov field, normalized by the particle volume, to obtain signals proportional to the complex refractive index. The complex normalized image used for the classification is expressed as:

$$E_{Rytovnorm} = \frac{\ln \sqrt{I} + i \cdot \varphi}{d^3} . \quad (4)$$

The architecture scheme is presented in Fig.3.a and detailed in methods and S7.

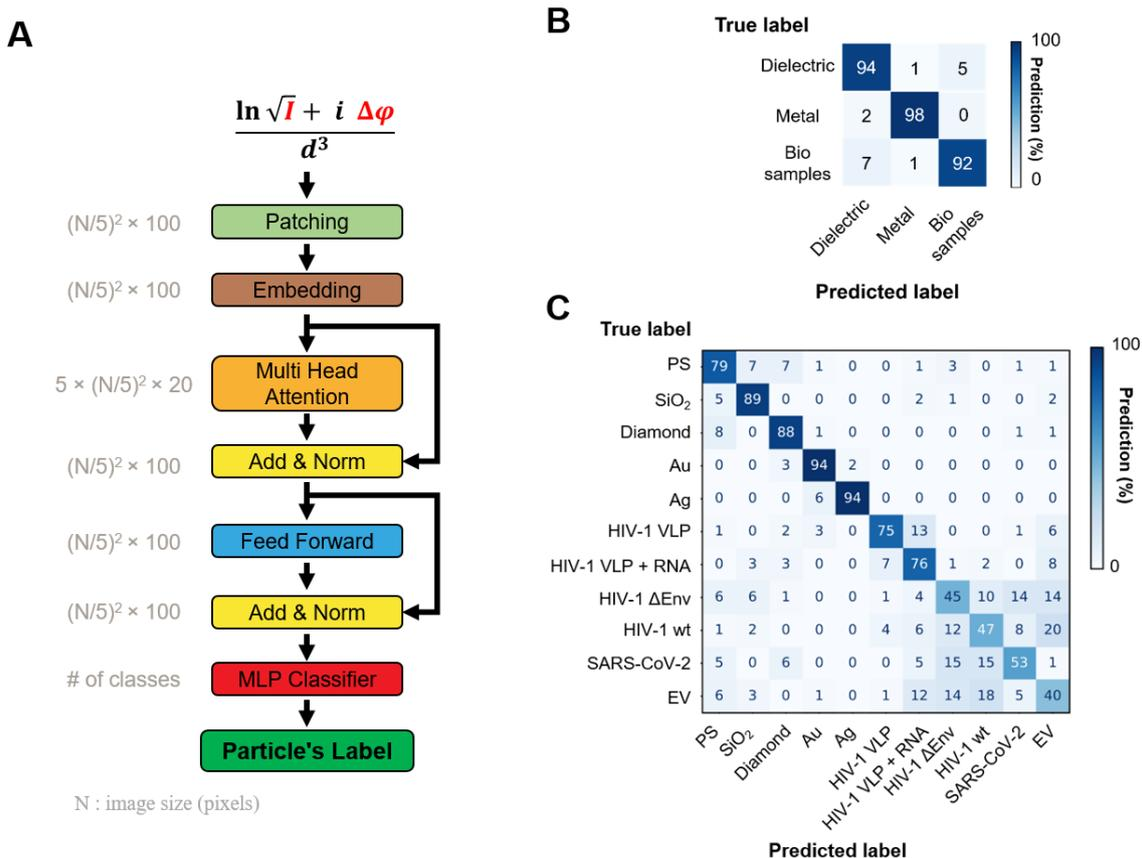


Figure 3: Machine Learning process. (A) Schema of Vision Transformer classification algorithm. (B) Confusion matrix of machine learning result for 3 main categories (dielectric, metal and biological samples). (C) Same as (b) with full particle nature classification

The particle classification capability of our algorithm can be assessed with the normalized confusion matrix (Figure 3.b,c). The algorithm precision is >92% to classify a particle either as dielectric, metallic or biological particle (Figure 3.b). More precision on the chemical and biological nature of the particle can also be obtained (Figure 3.c). In this paper, the chemical distinction inside dielectric (PS, SiO₂ and Diamond), or metallic (Au, Ag) classes reaches at least 79% with an average of 88%. For biological objects, different virus-like-particle (VLP), infectious virus (HIV-1, and SARS-CoV-2) with various subtype and extracellular vesicles (EVs) distinction is considered. Their nature is determined with an accuracy up to 75% for VLPs, and about 50% for others. The confusion between HIV-1 wt and HIV-1 ΔEnv (two different subtypes, see discussion) is comprehensible and predictable since HIV-1 ΔEnv contains multiple level of maturation of HIV-1, even a proportion of matured HIV-1 (similar to HIV-1 wt).^[51] Extracellular vesicles are also classified with moderate certainty, as expected for such heterogeneous class.

Interestingly, our deep learning algorithm gives comparable results regardless the number of training classes (comparison of Fig 3.c and Fig S5b-c), which is not usually the case with other classification methods such as regular k-means clustering. It suggests that the

complexity and generalization capabilities of our classification method is sufficient to handle all classes at the same time.

After identification of the particle nature, it is possible to extract more physical, chemical and biological information with limited bias. For example, for NPs, its refractive index $\tilde{n} = n + i \cdot n'$ can be retrieved from the SIR value of equation (2):

$$\tilde{n} = \sqrt{1 + \chi} = n_m + i n'_m + \frac{1}{n_m V_p} \left[-\frac{1}{2} \text{Re}(\text{SIR}) + i \text{Im}(\text{SIR}) \right], \quad (5)$$

where, χ the susceptibility of NP. The single particle tracking gives access to the hydrodynamic diameter. With the knowledge on the hydrodynamic layer thickness for the identified particle nature in the medium, the particle volume is then extracted from the core diameter.

Additionally, previous studies stated that the dry mass of biological materials is proportional to the optical volume difference.^[22–24] However, because the refractive index of virus is mostly higher than that of eukaryotic cell, the coefficient might be different from the literature review, and is discussed in S8. Hence, SIR analysis for viral particles allows to derive their dry mass.

2.6. Nanoparticle concentration measurement

3D volume of the field of view accessible with this method grants access in a single-shot to the concentration of the particles, independently with the particle nature. As explained before, the holographic imaging volume is fixed by the particle signal to noise ratio itself (see S6). In Fig.4.a, single shot particle concentrations have been determined over an imaging volume of 20-pL ($28 \times 28 \times 25 \text{-}\mu\text{m}^3$). Starting from an initial 100-nm PS solution of concentration of 1×10^{11} particles/mL (determined with a commercial Videodrop, Myriade, France), different dilutions (from 1:20 to 1:1000) were prepared and analyzed. Concentration measurements are obtained *via* counting the number of NP traces obtained in single time sequence acquisition (~ 300 images acquired at 400-Hz) and are in good agreement with the theoretical values, estimated from dilution proportions. We can extract concentration down to 1×10^8 particles/mL, or ≈ 0.16 -pM (about 1 particle per holographic volume) with a precision of 0.7×10^8 particles/mL (0.12-pM). On the opposite, the maximal concentration can reach up to 10^{11} particles/ml without changing our localization algorithm based on 3D projection volume into a single 2D image for particle pre-localization.

2.7. Identification and characterization of monodisperse nanoparticle solutions

Using RYMINI, we have studied monodisperse solutions containing dielectric (polystyrene, silica, diamond) or plasmonic (gold, silver) particles. In fig.4.b-c, a solution of 100-nm polystyrene (PS) nanoparticles has been imaged and both the complex refractive index of each particle and its size are presented. The hydrodynamic diameter is measured to be $d = 105 \pm 13$ nm which agrees with the information provided by the manufacturer, in which the average core size is 102 ± 3 nm, with a dispersion of 7.6 nm.

PS nanoparticles with size ranging from 60-nm to 200-nm have been studied with the same approach (Fig 4.d-f and Movie S2). We obtain a stability in the measured values for the

refractive index considering a hydrodynamic layer thickness of 10-nm, which agrees with the literature review (from 7-12nm^[52,53]). The complex refractive index has been measured $\tilde{n} = \left(1.610_{-0.095}^{+0.126}\right) + i \cdot \left(0.007_{-0.115}^{+0.102}\right)$ in agreement with the PS bulk refractive index at $\lambda = 450\text{nm}$,^[43] $\tilde{n}_{PS} = 1.6104 + i \cdot 6.33 \cdot 10^{-7}$, confirming no plasmonic effect on these particles. In addition, silica (SiO₂) and diamond di-electric nanoparticles as well as metallic gold (Au) and silver (Ag) nanoparticles were studied in Fig.4.g-i and Movie S3, and their statistics are summarized in the Table 1.

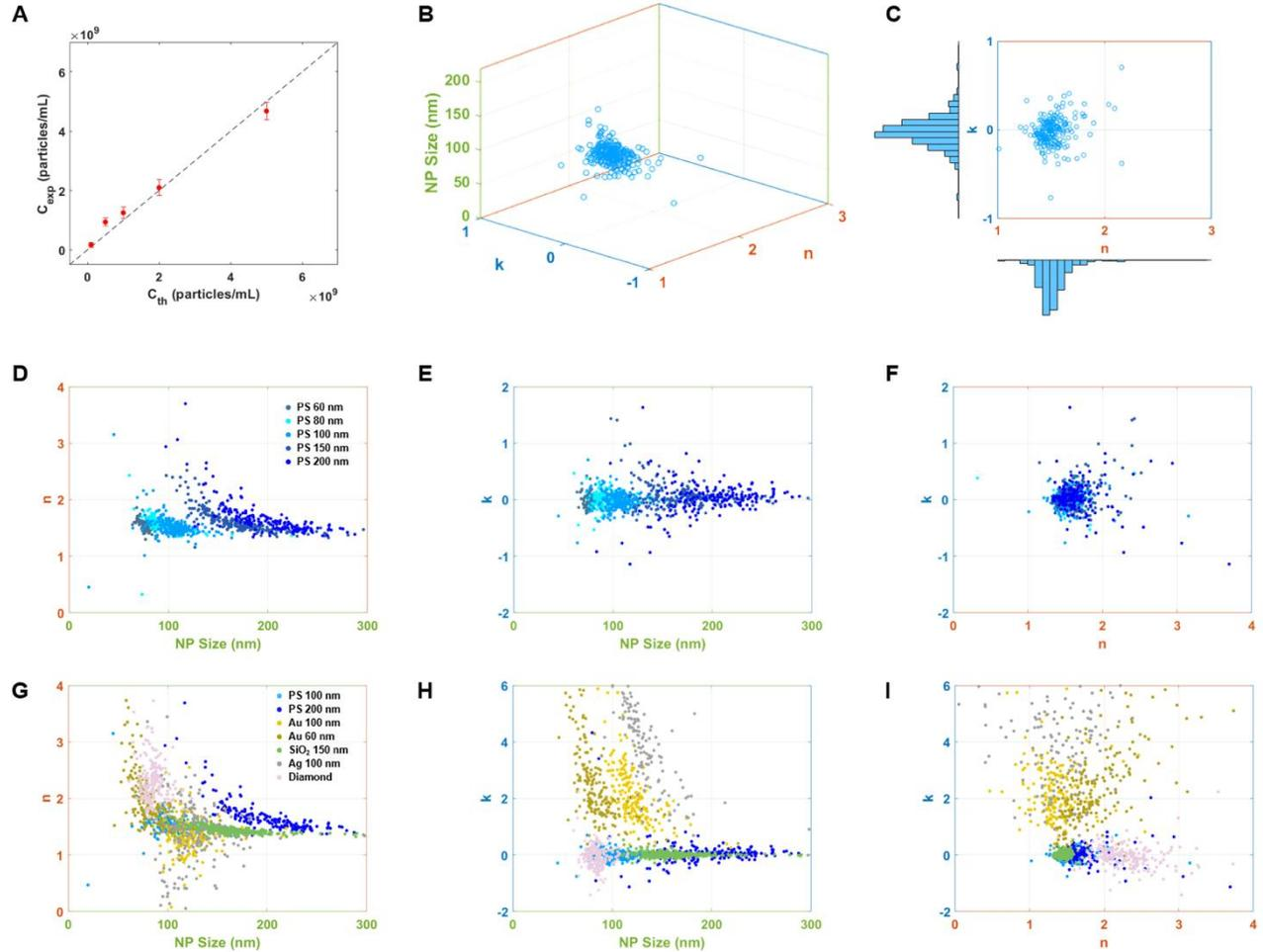


Figure 4: Quantification of individual NP in solution. (A) Single-shot concentration measurement (C_{exp}) of 100-nm PS solutions -made from dilutions of an initial solution- compared to the theoretical concentrations (C_{th}). Error bars represent the standard deviation of measurement. (B, C) Analysis of solution of 100-nm PS reveals size, complex refractive index. It is illustrated either in 3D (b) or in 2D graph (c). (D, E, F) Studies of different-sized PS nanoparticles with measured values for hydrodynamic size, real and imaginary refractive indices. (G, H, I) Measurements for different types of nanoparticles: dielectric (PS, Silica, Diamond) and metal NP (Au, Ag). Their responses are separated in the optical properties and size space, explaining the capability of machine learning segmentation.

Particles nature	Number of particles	Hydrodynamic Size (nm)	Refractive index n	Absorption coefficient k
PS	123	76.9 ^{+2.6} _{-2.2}	1.615 ^{+0.066} _{-0.061}	-0.052 ^{+0.091} _{-0.083}
	170	91.9 ^{+8.5} _{-6.4}	1.631 ^{+0.123} _{-0.078}	0.011 ^{+0.096} _{-0.079}
	221	105.1 ^{+8.2} _{-9.0}	1.556 ^{+0.106} _{-0.083}	-0.027 ^{+0.121} _{-0.115}
	228	167.8 ^{+20.5} _{-23.6}	1.605 ^{+0.185} _{-0.100}	0.029 ^{+0.109} _{-0.096}
	181	200.4 ^{+28.1} _{-28.0}	1.639 ^{+0.166} _{-0.122}	0.045 ^{+0.112} _{-0.142}
SiO ₂	105	124.9 ^{+15.7} _{-10.2}	1.476 ^{+0.053} _{-0.046}	0.046 ^{+0.064} _{-0.058}
	393	158.8 ^{+15.3} _{-13.0}	1.428 ^{+0.039} _{-0.029}	0.001 ^{+0.039} _{-0.035}
Diamond	208	84.6 ^{+4.0} _{-6.2}	2.241 ^{+0.223} _{-0.205}	-0.052 ^{+0.201} _{-0.175}
Au	201	79.6 ^{+12.1} _{-7.8}	1.805 ^{+0.304} _{-0.188}	2.136 ^{+1.032} _{-0.629}
	194	117.8 ^{+11.4} _{-7.1}	1.333 ^{+0.159} _{-0.101}	2.014 ^{+0.799} _{-0.491}
Ag	191	121.9 ^{+13.5} _{-14.0}	1.338 ^{+0.345} _{-0.268}	4.748 ^{+1.950} _{-1.497}

Table 1: Number of analyzed particles, Size, real, imaginary refractive index and electric susceptibility of various nano-particles.

For plasmonic particles, the light-matter interaction is very dependent with both the particle size and the working wavelength.^[45] The complex refractive index of 60-nm and 100-nm Au NP and 100-nm Ag NP have been studied and, according to Mie theory,^[54] their plasmon resonance wavelength are respectively 530-nm, 570-nm and 480-nm. The module of the complex refractive index is maximized when the wavelength is approaching the resonance and at the opposite is close to the refractive index of the bulk material when far from resonance. As an example, the refractive index of bulk gold and silver are tabulated^[44] at $\tilde{n}_{Au_{bulk}@450nm} = 1.38 + i \cdot 1.92$ and $\tilde{n}_{Ag_{bulk}@450nm} = 0.04 + i \cdot 2.65$ and the measured refractive index for 100-nm Au and Ag NP are $\tilde{n}_{Au_{100}} = \left(1.333^{+0.159}_{-0.101}\right) + i \cdot \left(2.014^{+0.799}_{-0.491}\right)$, closer to the bulk values far from resonance as compared to $\tilde{n}_{Ag_{100}} = \left(1.338^{+0.345}_{-0.268}\right) + i \cdot \left(4.748^{+1.950}_{-1.497}\right)$ closer to the NP plasmon resonance.

2.8. Characterization of polydisperse nanoparticle solutions

A polydisperse mixture of 200-nm PS and 100-nm Au NPs is prepared in order to demonstrate the discrimination of nanoparticle's nature by SIR analysis. These particles are chosen so that it is nearly impossible to identify each particle nature from its scattering intensity only, the values being almost similar at the working wavelength (fig.5.a and Movie S4). However, figure 5.a,b shows the graph of SIR analysis for the mixture in which two clusters can be segmented, not only by their size thank to tracking but also by their real and imaginary SIR value.

The machine learning classification determined that the particles in the mixture are mostly PS and Au (as shown in figure 5.c-d) as expected. Their concentrations are measured at $5.8 \pm 0.8 \times 10^8$ and $2.7 \pm 0.5 \times 10^8$ particles/mL respectively, in good agreement with the estimated values from manufacturer concentration and our dilution (5.0 and 3.8×10^8 particles/mL respectively). The other types of particles (SiO_2 , Diamond, Ag) identified by the automatized algorithm correspond to classification errors (5%), and we may conclude that our machine learning process achieves about 95% identification accuracy in this two particle-type mixture.

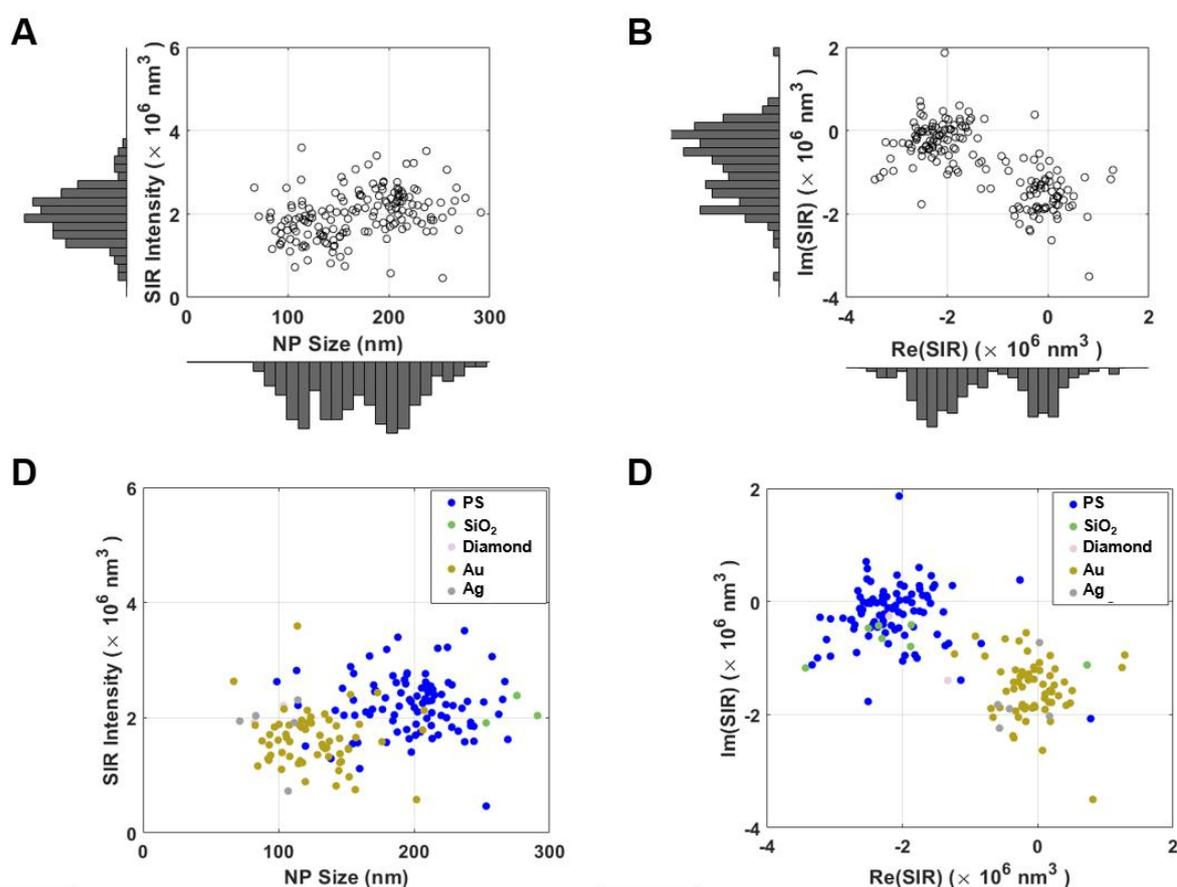


Figure 5: Analysis of polydisperse solution of 200-nm PS and 100-nm Au NP. (A, B) Graphs of analyzed particles show two possible clusters which are presented in the solution. **(C, D)** Automatized identification by machine learning.

2.9. Virus identification and characterization at the single particle level

We next challenged the RYMINI method to analyze biological nanoparticles in solutions: (i) artificial HIV-1 virus-like-particles (HIV-1 VLP) and VLP enriched in viral RNA (HIV-1 VLP+RNA), (ii) infectious HIV-1 particles (HIV-1 Wt) and HIV-1 pseudo-particles deprived of the surface Envelope Glycoproteins (HIV-1 Δ Env), (iii) infectious SARS-CoV-2, and (iv) extracellular vesicles (EV) excreted in cell culture (Fig.6.a). While EVs and VLP can be handled and measured without biohazard, measurements of infectious class 3 viruses such as HIV-1 and SARS-CoV-2 have to be performed in confined biological environments. The acquisitions of infectious samples were thus performed inside a biosafety cabinet of a confined level 3 biological laboratory (CEMIPAI, Montpellier, France) as shown in Fig.6.e (laser-beam safety panels have been removed to take the picture).

For biological samples, we have considered as pertinent to measure the size and mass (in Da) of each particle. The results for VLP, viruses and EVs are illustrated in Fig.6.b-d and reported in **Table 2**. HIV-1 VLP-GAG size analysis first validated the capabilities of our method, with a measured mean hydrodynamic diameter of 141^{+35}_{-17} -nm, which is the expected size of GAG-VLPs produced in higher eukaryotic cells.^[51,55] HIV-1 VLP-GAG particles enriched in viral RNA (HIV-1 VLP+RNA) showed an increased size of 179^{+25}_{-26} -nm, which correlates with the size modulation of viral RNA on VLP assembly.^[56] When moving to native, wt-infectious HIV-1 particles, the measured diameter (171^{+25}_{-17} -nm) was higher to that previously reported by CryoEM (145 ± 25 -nm).^[57] This is consistent since the particle size determined by EM are restricted to the outside of the lipid bilayer, therefore omitting the outer shell of the heavily glycosylated Gp160^{Env}, which should strongly participate in the hydrodynamic radius measured here. This was indeed confirmed by the measured size of HIV-1 Δ Env lacking the surface Env trimers (139^{+23}_{-14} -nm). SARS-CoV-2 size was found around $85.2^{+6.5}_{-9.4}$ -nm, which is consistent with sizes reported so far by CryoEM (91 ± 11 -nm)^[58] and AFM (89 ± 19 -nm).^[59] Finally, samples of extracellular vesicles showed a broader size range (233^{+54}_{-39} nm), as expected from these heterogeneous family of biological particles.^[60]

To convert each particle signal into mass, we used a β coefficient which only depends on the particle size at the first order (see S8). This simple assumption may lead to errors -especially for small and empty particles such as some extracellular vesicles- evaluated to be at maximum 200% for the determined mass (corresponding to 0.1 error in the refractive index value, see S9).

For HIV-1 wt, the dry mass, that we measured with optical signal (92^{+34}_{-24} MDa), is in good agreement with the dry mass estimated from the molecular composition analysis (90-102 MDa, see S9). For SARS-CoV-2, our dry mass determination is much lighter than the estimated value (31 MDa compared to 100 MDa). This disagreement

between two measurements may be attributed to the lack of information on SARS-CoV-2 composition and/or our hypothesis on the refractive index of SARS-CoV-2. Indeed, (i) from molecular composition, SARS-CoV-2 is found as heavy as HIV-1, even though it is 7 times smaller in volume; (ii) the refractive index law (see S8) has been determined from viruses and EVs that differ quite a lot in terms of structure when compared to SARS-CoV-2. Since SARS-CoV-2 is recently appeared in virology, further studies, including its refractive index, must be useful to improve the precision of dry mass determination .

Mass variations between all these biological nanoparticles correlate with their variations in size and content, with VLP-GAG + RNA > HIV-1 wt > HIV-1 Δ Env > VLP Gag > SARS-CoV-2. EVs can contain various biological material such as proteins and nucleic acids and showed an important heterogeneity in mass accordingly. Interestingly, molecular mass densities (in Da/nm³) confirmed that VLP-GAG and the EVs are less packed, while SARS-CoV-2 shows a slightly higher density. It suggests that SARS-CoV-2 packs its genome to form a denser supercoiled structure, as mentioned in previous studies.^[58,61-63] The dry mass density is found in between 0.05 to 0.14 g/mL. Supposing that the density of EVs and virus equals to the dry mass density plus the water density, our value agrees with the literature reviews.^[64] Altogether, these results demonstrate that the RYMINI is a powerful method to assess virus size, mass and densities; and can be used in high confinement laboratory for infectious virus analysis. However, it is important to remember that the mass is measured from an empiric law linking the virus refractive index with its size only, which is source of error.

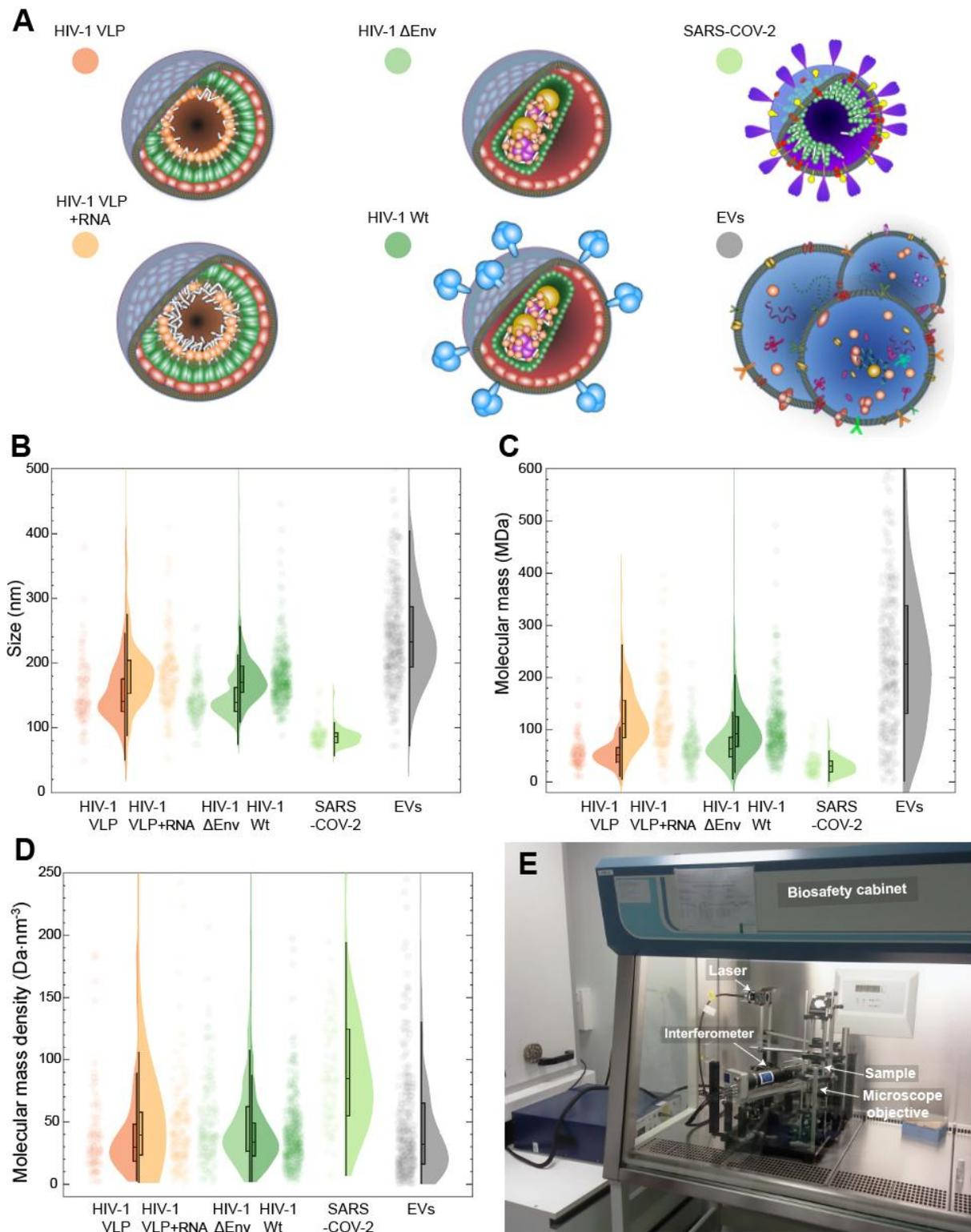


Figure 6: Quantification of biophysical parameters of virus and organic nano-objects. (A) Scheme of the different virus and virus-like-particles (VLP) analyzed in the experiment. (B, C, D) Characterization of biological samples: size, molecular dry mass (MDa) and molecular mass density ($\text{Da}\cdot\text{nm}^{-3}$). (E) Picture of the actual RYMINI microscope sitting in a biosafety cabinet in a L3 laboratory (laser safety protections removed to make the picture). Box plots represent: $\langle 5\%; 25\%; 50\%; 75\%; 95\% \rangle$

Particle nature	Number of particles	Hydrodynamic Size (nm)	Dry Mass (MDa)	Dry mass Density (Da.nm ⁻³)	Dry mass Density (g/mL)
HIV-1 VLP	90	141 ⁺³⁵ ₋₁₇	52 ⁺¹⁴ ₋₁₅	29.9 ^{+18.2} _{-11.6}	0.050 ^{+0.030} _{-0.019}
HIV-1 VLP + RNA	162	179 ⁺²⁵ ₋₂₆	111 ⁺⁴⁶ ₋₂₇	38.9 ^{+18.8} _{-15.6}	0.065 ^{+0.031} _{-0.026}
HIV-1 wt	337	171 ⁺²⁵ ₋₁₇	92 ⁺³⁴ ₋₂₄	33.6 ^{+15.6} _{-11.1}	0.056 ^{+0.026} _{-0.018}
HIV-1 ΔEnv	147	139 ⁺²³ ₋₁₄	64 ⁺²² ₋₁₆	38.9 ^{+23.2} _{-12.8}	0.065 ^{+0.039} _{-0.021}
SARS-CoV-2	88	85.2 ^{+6.5} _{-9.4}	31 ⁺¹⁰ ₋₁₃	84.5 ^{+40.2} _{-29.8}	0.140 ^{+0.067} _{-0.050}
Extracellular Vesicle	357	233 ⁺⁵⁴ ₋₃₉	227 ⁺¹¹² ₋₉₈	32.0 ^{+33.1} _{-16.5}	0.053 ^{+0.055} _{-0.027}

Table 2: Size, number of analyzed particles, Mass and density of various biological nano-objects

3. Conclusion

Our full optical RYMINI method unlocks identification and metrological characterization of nanoparticle solution at the single particle level without requiring *a priori* information on the sample nature. It grants access to the type of each detected particle as well as single-shot concentration, size, complex refractive index and mass (in gram and Dalton). For biological samples, the mass may carry errors due to some incomplete knowledge about the refractive index of the smallest virus. We have demonstrated its capability in monodisperse and polydisperse solutions of metallic and dielectric NP. The sample preparation as well as the acquisition are straightforward since large volumetric imaging is obtained in a single-shot manner with the RYMINI technique. To probe sub-pM concentration solutions, it requires less than one second and 10μL of solution, depending only on the imaging chamber volume. Our current sensitivity is compatible with identification and complete characterization of NP as small as 40-nm for metallic particles and 60-nm for dielectric particles (PS). The detection sensitivity could be pushed further by a change in the illumination scheme at the price of reducing the accessible imaging volume, or by attenuating the non-scattered light ^[65] but at the price of higher sensitivity to mechanical vibration and external light background, possibly problematic in demanding environment such as biosafety cabinet. Moreover, the label-free intrinsic signature of each particle can be used to quantify the homogeneity of particles in a non-invasive and biosafety-secured manner. The deployment of machine learning tools unlocks automatized identification of each detected particles. We believe that this method could be part of a system for routine pollution level or biological risk determination, NP metrology during production as well as fundamental viral studies.

4. Experimental Section and Methods

Optical setup. The setup is based on a homemade microscope using a quadriwave lateral shearing interferometer^[37,39] to measure the phase and the intensity of the beam. The sample is illuminated by a supercontinuum fiber laser (Leukos, France) filtered by a short-pass 700-nm dichroic and a 450 ± 10 nm optical filter (Thorlabs). A Köhler illumination has been made using one achromatic lens (75-mm, Thorlabs) and one aspherical lens (50-mm, Thorlabs). The image is formed with an oil-immersion objective Nikon Plan Fluor 100x NA 1.30 and a 400-mm achromat lens for the tube lens (Thorlabs). The total microscope magnification has been measured to be 205x, using a resolution test target (R3L1S4P, Thorlabs). The interferometer is composed of a Modified Hartmann Mask,^[66] a relay lens and a 2Me⁻ full-well capacity CMOS camera (Q-2HFW-hm, Adimec). The system is built on 40x30-cm breadboard and has a total height of 50-cm to be easily handled and introduced in biosafety cabinet.

Sample preparation. Perforated parafilm on a type 1.5 round coverslip plays the role of a 10 μ L imaging chamber. The parafilm is first heated up to 80°C so that it is slightly melted and sealed to the glass slide. After adding the solution, the chamber is closed by a second glass slide avoiding possible evaporation or leaks during handling.

Virus preparation. For HIV-1 and EVs production, 12.5 million of Human embryonic kidney cells (293THEK cell) were seeded in 10 ml of DMEM growth media 1 day before transfection. At 50-70% confluence, cells were transfected with calcium phosphate precipitate method, with 8 μ g total quantity of plasmid for either pcDNA3.1 (Mock), pHIV-1Gag^[67], pHIV-Psi-viralRNA^[68,69], pHIV-1(NL43) and pHIV-1Gag Δ Env^[51]. Cell culture supernatant containing viral particles was collected 48 hours post transfection. Supernatant was filtered through 0.45 μ m and then purified by ultracentrifugation on cushion of 25% sucrose - TNE buffer (10 mM Tris-HCl [pH 7.4], 100 mM NaCl, 1 mM EDTA) at 100000g, for 1 hour 30 minutes at 4°C, in SW32Ti Beckman Coulter rotor. Dry pellet was resuspended in TNE buffer at 4°C overnight.

For SARS-CoV-2 particle production, the strain BetaCoV/France/IDF0372/2020, was supplied by the National Reference Center for Respiratory Viruses hosted by Institut Pasteur (Paris, France) and headed by Pr. Sylvie van der Werf. The human sample from which strain BetaCoV/France/IDF0372/2020 was isolated has been provided by Dr. X. Lescure and Pr. Y. Yazdanpanah from the Bichat Hospital, Paris, France. Moreover, the BetaCoV/France/IDF0372/2020 strain was supplied through the European Virus Archive goes Global (EVAg) platform, a project that has received funding from the European Union's Horizon 2020 research and innovation program under the grant agreement No 653316. COV-2 Virus was propagated in VeroE6 cells with DMEM containing 2.5% FBS at 37°C with 5% CO₂ and harvested 72 hours post inoculation. Virus stocks were stored at -80°C and tittered using plaque assays as previously described^[59] and provided by CEMIPAI facility.

Data acquisition and analysis. A home-made program based on LabVIEW has been developed for both acquisition and processing. Between 200-300 frames per sample were acquired at 400-Hz with about 1.0 ms integration time (total acquisition time of \approx 700-ms) before being analyzed for single particle tracking. The analysis algorithm is performed offline with following the workflow: (i) to calculate the phase and intensity from each interferogram (raw camera image), including a flattening procedure (polynomial fit) of both intensity and phase maps to have an intensity centered at 1 and a

phase centered at 0; (ii) to generate a 3D stack from each intensity/phase couple using numerical propagation; (iii) to compute the Rytov intensity of each image in each stack; (iv) to pre-detect each particle on a maximum intensity projection along the propagation axis of the Rytov intensity stack; (v) to 3D superlocalize on the Rytov intensity stack each particle from its pre-detection using 3D Gaussian fitting; (vi) to extract a sub-pixel register at-the-focus intensity/phase image for each particle using the measured 3D position; (vii) to compute the DAI from the registered images and the particle size using the MSD from the temporal particle trace. Traces shorter than 20 images were deleted from the analyzed data to ensure a proper size measurement and DAI.

All statistics in the text and tables are in median and 25/75% percentile values.

The characteristics of the analysis computer is listed: AMD Ryzen 7 3800X 8-Core Processor, RAM 32Gb, graphic card NVIDIA GeForce RTX 2080Ti. It takes about 6 s/image to generated from the phase and intensity images (358×358 pixels) the full 3D volume and Z-axis maximum projection (2D image → 3D volume image → Z-axis maximum projection). The 3D numerical propagation is carried out for -15μm to + 15μm with step of 0.1μm (i.e. 301 planes). This was not parallelized on GPU and SoA 3D reconstruction as been demontstrated in a few ms (e.g. create 512×512×8 holographic volume in 10 ms^[70]). We thus expect the 3D reconstruction time to be reduced down to 50-100 ms (~100-fold faster).

The single particle tracking step is longer (multi-particle 3D tracking from Rytov image → create DAI images of each particle). In average, it takes about 5 second per particle per image. By moving to a GPU parallelized algorithm, it should allow to perform a whole reconstruction in about 1 minute for 30 particles in the field of view.

NP solution preparation. Multiple monodisperse solutions have been used in the experiment: regular polystyrene of 60, 80, 100 and 150-nm (Thermofisher), and calibration standard polystyrene of 100 and 200 nm (3K/4K Series Particle Counter Standards, Thermofisher Duke Standards), silica (Sigma Aldrich), Gold NP (Sigma Aldrich), Silver NP (Alfa Aesar), Diamond (Sigma Aldrich). When required, dilutions were performed with de-ionized water (18 MΩ m⁻¹).

Machine Learning architecture and hyper-parameters. Our Vision Transformer architecture, implemented with Adam optimizer, is composed of 3 different parts: the first one encodes the input images as patches; the second part allows to extract features using the scaled dot product attention; and the third part is a classic multi-layer perceptron to label each individual. The learning rate is initially set at 0.003 and evolved, following a triangular learning rate policy,^[71] with bound reduced by a factor of 0.85 after each 3 training epochs, in order to improve the training convergence. The model was trained during 30 epochs with a batch size of 20 Rytov images of 50×50 pixels and a cross-entropy loss function.

Received: ((will be filled in by the editorial staff))

Revised: ((will be filled in by the editorial staff))

Published online: ((will be filled in by the editorial staff))

References

- [1] B. Naseer, G. Srivastava, O. S. Qadri, S. A. Faridi, R. U. Islam, K. Younis, *Nanotechnology Reviews* **2018**, *7*, 623.
- [2] S. Mourdikoudis, R. M. Pallares, N. T. K. Thanh, *Nanoscale* **2018**, *10*, 12871.
- [3] H. Chugh, D. Sood, I. Chandra, V. Tomar, G. Dhawan, R. Chandra, *Artificial Cells, Nanomedicine, and Biotechnology* **2018**, *46*, 1210.
- [4] J. T. Trueb, O. Avci, D. Sevenler, J. H. Connor, M. S. Ünlü, *IEEE Journal of Selected Topics in Quantum Electronics* **2017**, *23*, 394.
- [5] R. Pecora, *Journal of Nanoparticle Research* **2000**, *2*, 123.
- [6] J. Stetefeld, S. A. McKenna, T. R. Patel, *Biophys Rev* **2016**, *8*, 409.
- [7] S. Zhu, L. Ma, S. Wang, C. Chen, W. Zhang, L. Yang, W. Hang, J. P. Nolan, L. Wu, X. Yan, *ACS Nano* **2014**, *8*, 10998.
- [8] S.-H. Lee, Y. Roichman, G.-R. Yi, S.-H. Kim, S.-M. Yang, A. van Blaaderen, P. van Oostrum, D. G. Grier, *Opt. Express, OE* **2007**, *15*, 18275.
- [9] A. Martinez-Marrades, J.-F. Rupprecht, M. Gross, G. Tessier, *Opt. Express* **2014**, *22*, 29191.
- [10] Y.-H. Lin, W.-L. Chang, C.-L. Hsieh, *Opt. Express, OE* **2014**, *22*, 9159.
- [11] M. Piliarik, V. Sandoghdar, *Nat Commun* **2014**, *5*, 4495.
- [12] C. Roose-Amsaleg, Y. Fedala, C. Vénien-Bryan, J. Garnier, A.-C. Boccara, M. Boccara, *Research in Microbiology* **2017**, *168*, 413.
- [13] A. D. Kashkanova, M. Blessing, A. Gemeinhardt, D. Soulat, V. Sandoghdar, *Nat Methods* **2022**, *19*, 586.
- [14] D. Midtvedt, F. Eklund, E. Olsén, B. Midtvedt, J. Swenson, F. Höök, *Analytical Chemistry* **2020**, *92*, 1908.
- [15] B. Midtvedt, E. Olsén, F. Eklund, F. Höök, C. B. Adiels, G. Volpe, D. Midtvedt, *ACS Nano* **2021**, *15*, 2240.
- [16] V. Turkki, E. Alppila, S. Ylä-Herttuala, H. P. Lesch, *Viruses* **2021**, *13*, 939.
- [17] L. Saemisch, N. F. van Hulst, M. Liebel, *Nano Lett.* **2021**, *21*, 4021.
- [18] B. Špačková, H. Klein Moberg, J. Fritzsche, J. Tenghamn, G. Sjösten, H. Šípová-Jungová, D. Albinsson, Q. Lubart, D. van Leeuwen, F. Westerlund, D. Midtvedt, E. K. Esbjörner, M. Käll, G. Volpe, C. Langhammer, *Nat Methods* **2022**, *19*, 751.
- [19] U. Ortiz-Orruño, R. Quidant, N. F. van Hulst, M. Liebel, J. Ortega Arroyo, *ACS Nano* **2023**, *17*, 221.
- [20] G. G. Daaboul, A. Yurt, X. Zhang, G. M. Hwang, B. B. Goldberg, M. S. Ünlü, *Nano Lett.* **2010**, *10*, 4727.
- [21] Q. Xia, Z. Guo, H. Zong, S. Seitz, C. Yurdakul, L. Wang, J. H. Connor, J.-X. Cheng, **2022**, DOI 10.48550/arXiv.2212.10521.
- [22] R. Barer, *Nature* **1952**, *169*, 366.
- [23] B. Rappaz, E. Cano, T. Colomb, J. Köhn, C. Depeursinge, V. Simanis, P. J. Magistretti, P. Marquet, *Journal of Biomedical Optics* **2009**, *14*, 034049.

- [24] S. Aknoun, J. Savatier, P. Bon, F. Galland, L. Abdeladim, B. Wattellier, S. Monneret, *Journal of Biomedical Optics* **2015**, *20*, 126009.
- [25] M. Mir, Z. Wang, Z. Shen, M. Bednarz, R. Bashir, I. Golding, S. G. Prasanth, G. Popescu, *Proc. Natl. Acad. Sci. U.S.A.* **2011**, *108*(32), 13124.
- [26] G. Young, N. Hundt, D. Cole, A. Fineberg, J. Andrecka, A. Tyler, A. Olerinyova, A. Ansari, E. G. Marklund, M. P. Collier, S. A. Chandler, O. Tkachenko, J. Allen, M. Crispin, N. Billington, Y. Takagi, J. R. Sellers, C. Eichmann, P. Selenko, L. Frey, R. Riek, M. R. Galpin, W. B. Struwe, J. L. P. Benesch, P. Kukura, *Science* **2018**, *360*, 423.
- [27] E. D. B. Foley, M. S. Kushwah, G. Young, P. Kukura, *Nat Methods* **2021**, *18*, 1247.
- [28] F. Lampert, G. F. Bahr, A. S. Rabson, *Science* **1969**, *166*, 1163.
- [29] G. F. Bahr, W. D. Foster, D. Peters, E. H. Zeitler, *Biophysical Journal* **1980**, *29*, 305.
- [30] E. de Hoffmann, V. Stroobant, *Mass Spectrometry: Principles and Applications*, John Wiley & Sons, **2007**.
- [31] Z. Nie, Y.-K. Tzeng, H.-C. Chang, C.-C. Chiu, C.-Y. Chang, C.-M. Chang, M.-H. Tao, *Angewandte Chemie* **2006**, *118*, 8311.
- [32] N. Arjmandi, W. Van Roy, L. Lagae, *Analytical Chemistry* **2014**, *86*, 4637.
- [33] A. Y. Ozkumur, F. E. Kanik, J. T. Trueb, C. Yurdakul, M. S. Ünlü, *IEEE Journal of Selected Topics in Quantum Electronics* **2019**, *25*, 1.
- [34] S. M. Scherr, D. S. Freedman, K. N. Agans, A. Rosca, E. Carter, M. Kuroda, H. E. Fawcett, C. E. Mire, T. W. Geisbert, M. S. Ünlü, J. H. Connor, *Lab Chip* **2017**, *17*, 917.
- [35] P. Langehanenberg, G. von Bally, B. Kemper, *3D Res* **2011**, *2*, 4.
- [36] P. Bon, N. Bourg, S. Lécart, S. Monneret, E. Fort, J. Wenger, S. Lévêque-Fort, *Nat. Commun.* **2015**, *6*, 7764.
- [37] P. Bon, G. Maucort, B. Wattellier, S. Monneret, *Opt. Express* **2009**, *17*, 13080.
- [38] P. Bon, S. Lécart, E. Fort, S. Lévêque-Fort, *Biophys. J.* **2014**, *106*, 1588.
- [39] J. Primot, L. Sogno, *J. Opt. Soc. Am. A, JOSAA* **1995**, *12*, 2679.
- [40] A. Barty, K. A. Nugent, D. Paganin, A. Roberts, *Opt. Lett.* **1998**, *23*, 817.
- [41] H. Sierra, C. A. DiMarzio, D. H. Brooks, *JOSA A, Vol. 26, Issue 5, pp. 1268-1276* **2009**, *26*, 1268.
- [42] P. Bon, B. Wattellier, S. Monneret, *Opt. Lett., OL* **2012**, *37*, 1718.
- [43] X. Zhang, J. Qiu, J. Qiu, J. Qiu, X. Li, X. Li, J. Zhao, J. Zhao, L. Liu, L. Liu, *Appl. Opt., AO* **2020**, *59*, 2337.
- [44] P. B. Johnson, R. W. Christy, *Physical Review B* **1972**, *6*, 4370.
- [45] S. Khadir, S. Khadir, D. André, P. C. Chaumet, S. Monneret, N. Bonod, M. Käll, A. Sentenac, G. Baffou, *Optica, OPTICA* **2020**, *7*, 243.
- [46] H. Qian, M. P. Sheetz, E. L. Elson, *Biophysical Journal* **1991**, *60*, 910.
- [47] V. Brasiliense, A. N. Patel, A. Martinez-Marrades, J. Shi, Y. Chen, C. Combellas, G. Tessier, F. Kanoufi, *Journal of the American Chemical Society* **2016**, *138*, 3478.
- [48] A. Vaswani, N. Shazeer, N. Parmar, J. Uszkoreit, L. Jones, A. N. Gomez, Ł. Kaiser, I. Polosukhin, in *Advances in Neural Information Processing Systems*, Curran Associates, Inc., **2017**.
- [49] A. Dosovitskiy, L. Beyer, A. Kolesnikov, D. Weissenborn, X. Zhai, T. Unterthiner, M. Dehghani, M. Minderer, G. Heigold, S. Gelly, J. Uszkoreit, N. Houlsby, **2021**, DOI 10.48550/arXiv.2010.11929.
- [50] C. Trabelsi, O. Bilaniuk, Y. Zhang, D. Serdyuk, S. Subramanian, J. F. Santos, S. Mehri, N. Rostamzadeh, Y. Bengio, C. J. Pal, **2018**.
- [51] C. Floderer, J.-B. Masson, E. Boilley, S. Georgeault, P. Merida, M. El Beheiry, M. Dahan, P. Roingeard, J.-B. Sibarita, C. Favard, D. Muriaux, *Sci Rep* **2018**, *8*, 16283.
- [52] S. Sasaki, *Colloid & Polymer Sci* **1984**, *262*, 406.
- [53] G. K. Min, M. A. Bevan, D. C. Prieve, G. D. Patterson, *Colloids and Surfaces A: Physicochemical and Engineering Aspects* **2002**, *202*, 9.

- [54] G. Mie, *Annalen der Physik* **1908**, 330, 377.
- [55] A. J. Smith, M. I. Cho, M. L. Hammarskjöld, D. Rekosh, *Journal of Virology* **1990**, 64, 2743.
- [56] C. Faivre-Moskalenko, J. Bernaud, A. Thomas, K. Tartour, Y. Beck, M. Iazykov, J. Danial, M. Lourdin, D. Muriaux, M. Castelnovo, *PLOS ONE* **2014**, 9, e83874.
- [57] J. A. G. Briggs, T. Wilk, R. Welker, H.-G. Kräusslich, S. D. Fuller, *EMBO J* **2003**, 22, 1707.
- [58] Z. Ke, J. Oton, K. Qu, M. Cortese, V. Zila, L. McKeane, T. Nakane, J. Zivanov, C. J. Neufeldt, B. Cerikan, J. M. Lu, J. Peukes, X. Xiong, H.-G. Kräusslich, S. H. W. Scheres, R. Bartenschlager, J. A. G. Briggs, *Nature* **2020**, 588, 498.
- [59] S. Lyonnais, M. Hénaut, A. Neyret, P. Merida, C. Cazevielle, N. Gros, C. Chable-Bessia, D. Muriaux, *Sci Rep* **2021**, 11, 11885.
- [60] E. Willms, C. Cabañas, I. Mäger, M. J. A. Wood, P. Vader, *Frontiers in Immunology* **2018**, 9.
- [61] B. Turoňová, M. Sikora, C. Schürmann, W. J. H. Hagen, S. Welsch, F. E. C. Blanc, S. von Bülow, M. Gecht, K. Bagola, C. Hörner, G. van Zandbergen, J. Landry, N. T. D. de Azevedo, S. Mosalaganti, A. Schwarz, R. Covino, M. D. Mühlebach, G. Hummer, J. Krijnse Locker, M. Beck, *Science* **2020**, 370, 203.
- [62] H. Yao, Y. Song, Y. Chen, N. Wu, J. Xu, C. Sun, J. Zhang, T. Weng, Z. Zhang, Z. Wu, L. Cheng, D. Shi, X. Lu, J. Lei, M. Crispin, Y. Shi, L. Li, S. Li, *Cell* **2020**, 183, 730.
- [63] C. Wu, W. Yin, Y. Jiang, H. E. Xu, *Acta Pharmacol Sin* **2022**, 43, 3021.
- [64] K. Brennan, K. Martin, S. P. FitzGerald, J. O’Sullivan, Y. Wu, A. Blanco, C. Richardson, M. M. Mc Gee, *Sci Rep* **2020**, 10, 1039.
- [65] C.-Y. Cheng, Y.-H. Liao, C.-L. Hsieh, *Nanoscale* **2019**, 11, 568.
- [66] J. Primot, N. Guérineau, *Appl. Opt.* **2000**, 39, 5715.
- [67] A. de Poret, R. Dibsy, P. Merida, A. Trausch, K. Inamdar, D. Muriaux, *Biology of the Cell* **2022**, 114, 259.
- [68] R. Zufferey, D. Nagy, R. J. Mandel, L. Naldini, D. Trono, *Nat Biotechnol* **1997**, 15, 871.
- [69] L. Naldini, U. Blömer, P. Gallay, D. Ory, R. Mulligan, F. H. Gage, I. M. Verma, D. Trono, *Science* **1996**, 272, 263.
- [70] M. C. Nguyen, P. Berto, F. Valentino, F. Kanoufi, G. Tessier, *Optics Express* **2022**, DOI 10.1364/OE.463115.
- [71] L. N. Smith, in *2017 IEEE Winter Conference on Applications of Computer Vision (WACV)*, **2017**, pp. 464–472.

Funding

This work was supported by CNRS. This project has received funding from the European Research Council (ERC) under the European Union’s Horizon 2020 research and innovation programme (grant agreement No. [848645]).

Author contributions

MCN and PBon designed the experiment, wrote the acquisition and analysis code. MCN built the optical setup and performed the acquisitions and analysis. PBonnaud and GM wrote the deep learning algorithm. RD performed cell culture, infection, sample preparation of viruses. SL helped setting up the material in BSL3; SL, DM, MCN and PBon performed the experiments in the BSL3. MCN, SL, DM and PBon wrote the manuscript. DM and PBon raised funding. All authors discussed the data and agreed on the final manuscript.

Competing interests

MCN salary has been financed by the French company *Myriade* between 01/2020 and 05/2021. All other authors declare they have no competing interests.

Data and materials availability

Raw intensity and phase data are available upon reasonable request to the corresponding authors. Self-executable are provided along with test data setup (PS100 nm) and readme on the repository: doi.org/10.5281/zenodo.7576246

Supporting Information

This PDF file includes:

Supplementary Text

Figs. S1 to S6

References

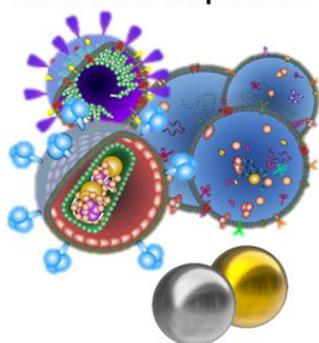
Other Supplementary Material for this manuscript includes the following: Movies S1 to S4

Table of Contents

Label-free single nanoparticle identification and characterization in demanding environment, including infectious emergent virus

Minh-Chau Nguyen, Peter Bonnaud, Rayane Dibsy, Guillaume Maucort, Sébastien Lyonnais, Delphine Muriaux, Pierre Bon

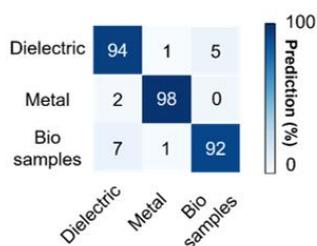
Label-free nanoparticles



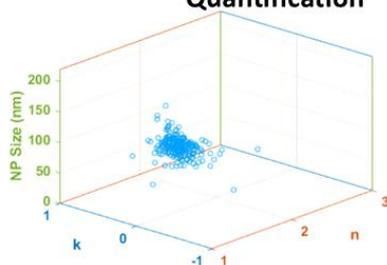
Demanding environment



Automatized identification



Quantification



Label-free single nanoparticle identification and quantitative characterization are unlocked through the study of brownian motion and highly-stable quantitative phase and intensity optical imaging. We demonstrate the detection and analysis of nanoparticles in solution, including infectious virus (HIV-1, SARS-CoV-2) observed in level-3 confined laboratory.